Printing Nanostructures with a Propelled Anti-Pinning Ink Droplet

*Gady Konvalina, Alexander Leshansky, and Hossam Haick**

Striving for cheap and robust manufacturing processes has prompted efforts to adapt and extend methods for printed electronics and biotechnology. A new "direct-write" printing method for patterning nanometeric species in addressable locations has been developed, by means of evaporative deposition from a propelled anti-pinning ink droplet (PAPID) in a manner analogous to a snail-trail. Three velocity-controlled deposition regimes have been identified; each spontaneously produces distinct and well-defined self-assembled deposition patterns. Unlike other technologies that rely on overlapping droplets, PAPIDs produce continuous patterns that can be formed on rigid or flexible substrates, even within 3D concave closed shapes, and have the ability to control the thickness gradient along the pattern. This versatile low cost printing method can produce a wide range of unusual electronic systems not attainable by other methods.

1. Introduction

The need to deploy thin film patterns on surfaces – with ever increasing demands for cheap robust manufacturing processes – has driven extensive efforts to adapt ink printing methods, such as ink-jet, screen printing, and contact printing,[1–4] for many printed electronics applications.[5] The adoption of printing methods in widespread manufacturing of printed electronics requires the following methods to be possible: 1) deposition of materials in addressable locations; 2) printing over a variety of materials, in particular those incompatible with standard lithographic processes (e.g., organic materials); 3) flexibility of pattern design; and 4) patterning large areas at low costs.[2] So far, properly adapted printing techniques have been shown to be useful for fabrication of printed organic electronic devices,[6,7] sensors,[8] photovoltaics,[9] micromechanical devices,[10] organic,[3] and inorganic[11] light-emitting diode (LED) displays. Adaptations included: 1) ink property adjustments to comply with the requirements of the solute, printed substrate, and/or delivery system;[1,10] 2) surface pre-treatments to tune ink wettability and ultimately improve pattern quality;[10,12] and 3) post-printing treatments to cure the deposited patterns.[1,12] For most printing methods, the printed surface geometry must be planar since the printing configuration relies on a fixed spatial alignment between the delivery system and the printed surface.[10] A few methods avoid this limitation by using special inks and alternative printing heads.[13] For example, highly concentrated viscous inks of metal nanoparticles (NPs) extruded from a nozzle allow high aspect ratio 3D structures to be formed. Nevertheless, printing surfaces with restricted spatial access, such as within tube-like shapes, is not a trivial issue. Nozzle clogging problems caused by the high solid loading of the inks must also be addressed.[10,13]

We present a conceptually new method to deposit and pattern nanometric species. The concept is based on "propelled anti-pinning ink droplets" (PAPIDs) that perform evaporative deposition[14] along their actuation path, analogous to the trail pattern left behind a snail. In this approach, a binary combination of solvents is used to adjust ink properties and flow characteristics to achieve functional droplets that conform to the surface, while allowing easy lateral manipulation and patterning. By applying actuating forces, such as gravity, via surface inclination[15] or gas shear stress,[16] PAPIDs can be actuated over different types of surfaces to accomplish deposition patterns, even on 3D curved surfaces, without the need for special printing heads, tips, or capillary nozzles. The governing parameters and resultant patterns of 3 distinct deposition modes are characterized and representative working devices are fabricated to demonstrate the potential applications of PAPIDs in printed electronics and sensors.

2. Results and Discussion

2.1. Working Principle

Unlike conventional ink droplets that pin to the surface upon contact,[8] PAPIDs have been designed to allow the ink droplets to be laterally actuated while conforming to the geometry of the substrate, and producing distinct and controllable deposition patterns (**Figure 1**). This combination of functions is made possible by the binary solvent composition of our ink (see Supporting Information, Table S1). The binary composition induces solutal Marangoni[17] vortices within the ink droplets in the direction opposing droplet spreading (Figure 1a).[18] The vortices are produced by surface tension gradients generated by concentration gradients following enhanced evaporation of the more volatile compound near the fluid/substrate contact line. For example, a combination of toluene and nonane

Dr. G. Konvalina, Prof. A. Leshansky, Prof. H. Haick
The Department of Chemical Engineering and Russell Berrie Nanotechnology Institute
Technion – Israel Institute of Technology
Haifa 3200003, Israel
E-mail: hhossam@technion.ac.il

DOI: 10.1002/adfm.201500215

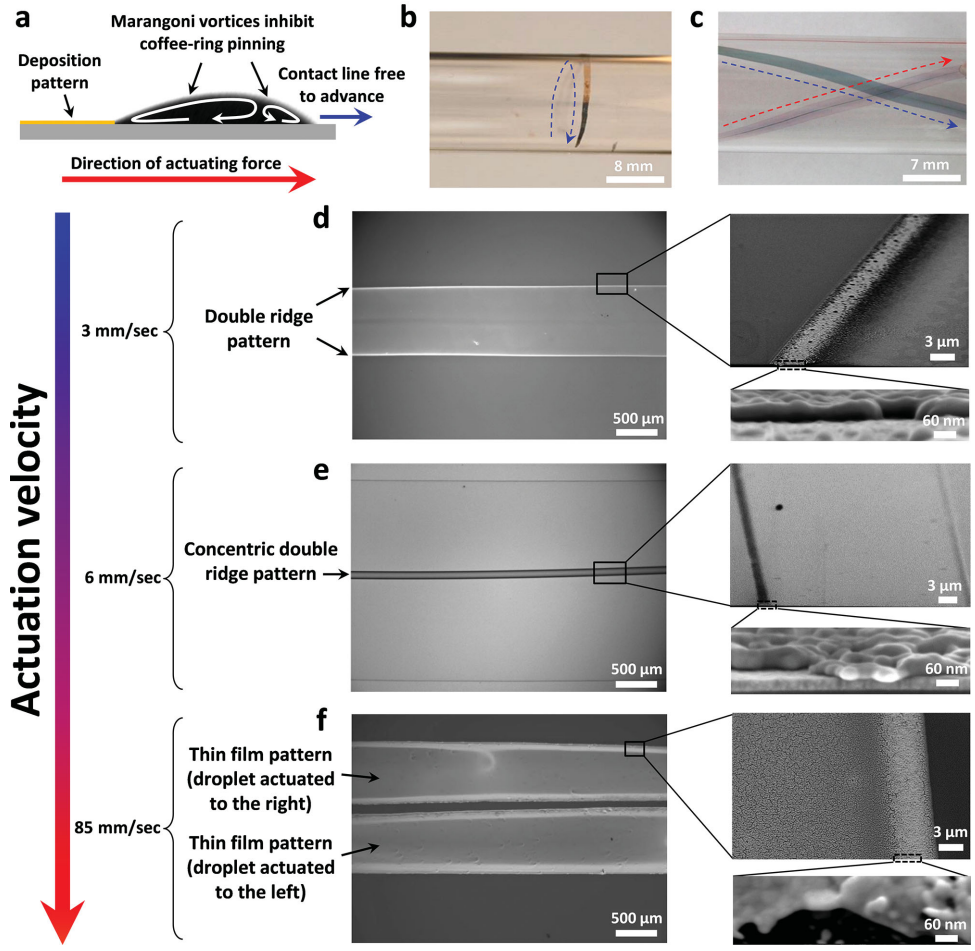

Figure 1. a) Schematic diagram of a laterally actuated ink droplet having a binary solvent composition that induces solutal Marangoni vortices, which prevent coffee-ring pinning while allowing deposition of solids at the rear; optical micrographs of glass tubes printed with gold lines on the b) outside and c) inside surface, using gold nanoparticles (Au-NPs) based PAPIDs actuated by surface inclination. Optical micrographs (left) and HR-SEM images (right) of d) a parallel double ridge pattern left behind a PAPID actuated by surface inclination, e) a parallel double ridge pattern with an additional concentric double ridge pattern formed behind a PAPID actuated by surface inclination, and f) 2 parallel thin-film line patterns left behind 2 PAPIDs actuated using gas shear stress. The arrow on the left illustrates the transition between pattern types along with the increase in droplet lateral velocity, including actual velocities for the gold patterns seen in (d), (e), and (f).

leads to a decrease in the toluene concentration near the contact line (since its vapor pressure, 3.8 kPa, is substantially larger than that of nonane, 0.4 kPa) and thus to a decrease in the local surface tension (from ≈30 mN m^{-1} for a toluene-rich solution with nonane to ≈24 mN m^{-1} with toluene almost completely depleted). Surface tension decrease at the contact line then causes the liquid to flow from the contact line towards the center along the liquid/air interface. This flow induces Marangoni vortices within the droplet, inhibiting spreading of the droplet without substantially increasing its contact angle θ with the surface (<12° for a Si surface, see Supporting Information, Figure S1a). The vortices prevent coffee-ring pinning[19,20] (Figure 1a and Supporting Information, Figure S1a) and lower the contact angle hysteresis $\Delta\theta$ (see Supporting Information, Figure S1b) enabling lateral actuation of the droplets when subjected to an actuating force, such as gravity (i.e., surface inclination; see Supporting Information, Figure S2a,b and Movie S1) or gas shear stress (see Supporting Information, Figure S3a,b). This is why actuation of unary solvent-based ink droplets does not occur under the same actuating forces. Since θ also remains small despite the anti-spreading direction of the vortices, the droplets stick to the surface and undergo evaporative deposition,[14] consequently allowing printing over 3D curved surfaces (Figure 1b,c). Determined by the lateral actuation velocity, ink droplets can be propelled in 4 different flow regimes, 3 producing distinct and controllable self-assembled deposition patterns (Figure 1d–f).

2.2. Flow Regimes Characterization

To understand the governing factors of the resultant deposition patterns, it is first imperative to characterize the 4 flow regimes of the PAPIDs. Therefore, we classified these based on the observations of PAPIDs (with a volume range between 0.2 and 1.5 µL) running down an inclined surface[15] or actuated by

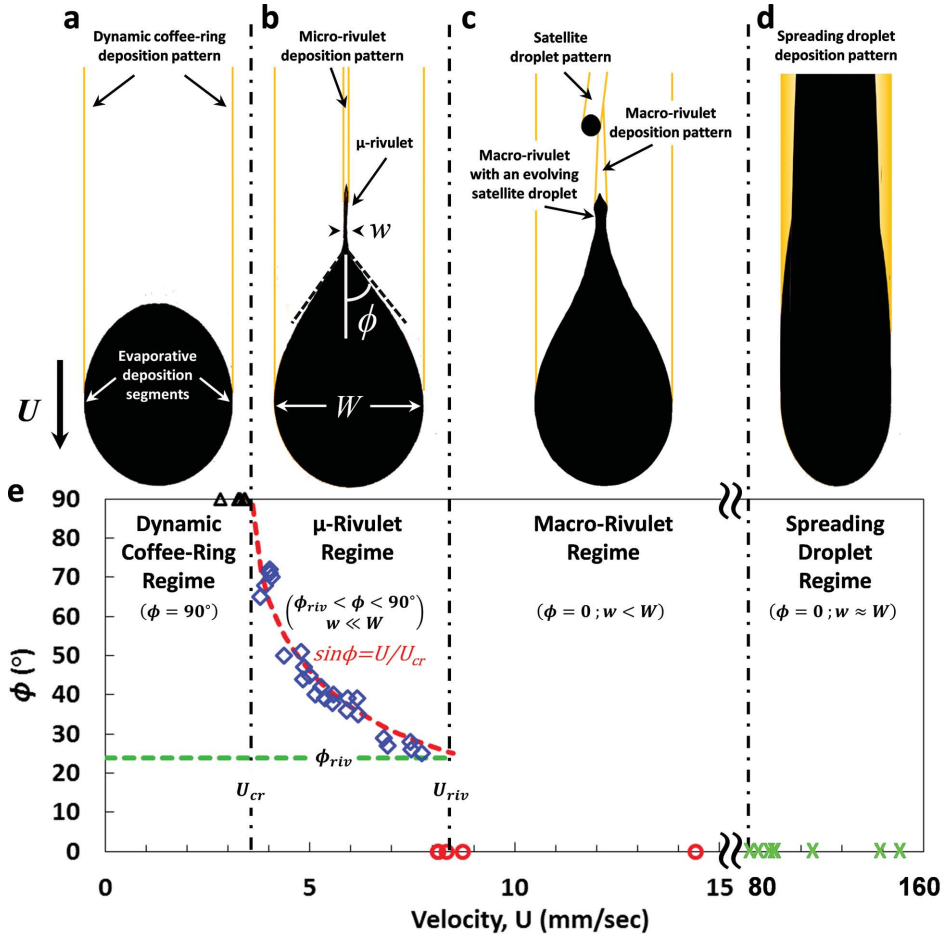

Figure 2. Schematic diagrams of the 4 flow regimes: a) dynamic coffee-ring; b) μ-rivulet; c) macro-rivulet; and d) spreading droplet, with the related geometric characteristics of the droplet contact line contours and resultant deposition patterns indicated. e) Flow regime map showing the relation between ϕ and U for ink droplets flowing over a Si substrate under the 4 flow regimes, dynamic coffee-ring (black triangles), μ-rivulet (blue diamonds), macro-rivulet (red circles), and spreading droplet (green x symbols). Ink droplet volumes ranged between 0.2–1.5 μL and were actuated using surface inclinations between 14–45° in the case of the first 3 regimes and gas shear stress using airflow between 1–2.5 L min^{-1} for the spreading droplet regime. Note: Using gas shear stress actuation, the first 3 flow regimes were obtained in similar velocity ranges as in the surface inclination experiments.

gas shear stress (see the Supporting Information, Methods section).[16] The classification is based on the velocity, U, of the ink droplet and geometric characteristics of both the contact line contours and resultant deposition patterns (**Figure 2**). At low velocities (2.7–3.4 mm s^{-1}), ink droplets produce a characteristic double-ridge pattern in a process we call "dynamic coffee-ring deposition" (see Supporting Information, Movie S2). Such droplets maintain a nearly circular or oval-shaped contact line for which the angle ϕ between the receding contact line and the velocity preserves a value of 90° (Figure 2a,e).[14,21]

Above a critical velocity ($U_{cr} \approx 3.6$ mm s^{-1}), the receding contact line deforms into a corner shape, with the opening angle ϕ decreasing with U (Figure 2b). The relation between ϕ and U is consistent (Figure 2e) with the phenomenological law

$$\sin\phi = \frac{U}{U_{cr}} \quad (1)$$

where U determines the ϕ that maintains a constant velocity (U_{cr}) in the direction normal to the contact line.[21] In the case of the reported PAPIDs, a micro-rivulet (μ-rivulet) protrudes from this corner and trails the droplet (a novel observation). This μ-rivulet deposits an additional double-ridge pattern concentric to the 2 dynamic coffee-ring ridges (Figure 1e) in a process we have called "μ-rivulet deposition" (see Supporting Information, Movie S3). The width w of such μ-rivulets is on the order of ≈10% of the width (W) of the droplet and decreases with U (see Supporting Information, Figure S4). These observations suggest that the occurrence of the μ-rivulet is related to the binary composition of the ink, since we saw formation of such μ-rivulets for pure binary-solvent droplets (see Supporting Information, Movie S4), but not for unary-solvent droplets. The capillary stability of the μ-rivulet and the prevention of pearling[21] is also attributed to the binary composition. We suggest that at the μ-rivulet contact lines, the component with the higher surface tension, γ, evaporates faster; therefore, γ decreases locally during evaporation, maintaining a stable contact line.

When the velocity is increased above a critical velocity, U_{riv}, with a corresponding critical opening angle, ϕ_{riv}, the corner shape

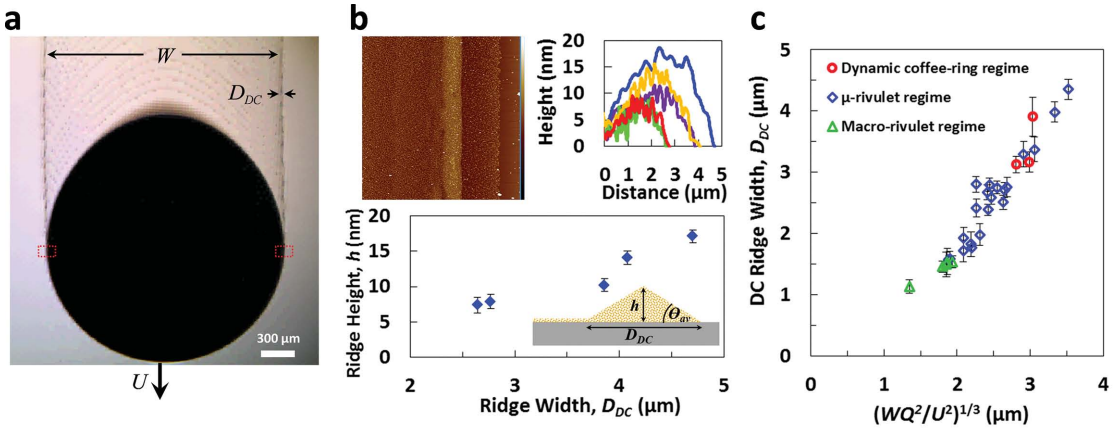

Figure 3. a) Optical micrograph of a PAPID flowing down an inclined Si wafer, leaving behind a dynamic coffee-ring pattern of Au NPs. The droplet velocity (U), width (W), ridge width of the dynamic coffee-ring pattern (D_{DC}), and 2 deposition segments (red rectangles) are depicted. b) AFM analysis of dynamic coffee-ring ridges showing (top left) a 20 × 20 μm scan of a characteristic NPs ridge (color scale range between 0–60 nm); (top right) height profiles of 5 representative ridges, and (bottom) maximum ridge height versus ridge width of the 5 ridges with the inset schematically illustrating a simplified triangular cross-section ridge profile. c) Plot showing D_{DC} versus $(WQ^2/U^2)^{1/3}$ for PAPIDs actuated under the 3 flow regimes that produce the dynamic coffee-ring pattern: dynamic coffee-ring (red circles), μ-rivulet (blue diamonds), and macro-rivulet (green triangles). PAPIDs volumes ranged between 0.3–1.5 μL and were actuated at surface inclinations between 14–45°.

at the rear of the droplet opens and a characteristic unstable macro-rivulet is formed, for which ϕ is assigned a value of zero (Figure 2c). These findings indicate that the transition occurs at $U_{riv} \approx 7.9$ mm s^{-1} and $\phi_{riv} \approx 25°$ (Figure 2e). The transition values are consistent with our calculations based on the lubrication theory,[21] which predicts a ϕ_{riv} of ≈24°, from which U_{riv} can be deduced by applying (1), giving a value of ≈8.9 mm s^{-1} (see the Supporting Information, Section 3). The width w of macro-rivulets increases with U towards the width W of the droplet.[21] Nevertheless, since macro-rivulets are unstable and undergo pearling, producing satellite droplets from the rear (see Supporting Information, Movie S5), the resultant patterns are complex, uncontrollable and, as a result, not applicable for printing.

At yet higher values of U (>80 mm s^{-1}) and/or for PAPIDs with high viscosity (at large capillary numbers, $Ca = U\eta/\gamma > 2 \times 10^{-3}$, where η is the viscosity of the liquid), the droplet deforms into an elongated thin film[22] that evaporates and leaves behind a uniform thin-film deposit in a process we have called "spreading droplet deposition" (Figure 2d). In this flow process, the trailing contact line is left behind while the advancing contact line spreads out in the direction of the applied actuation force forming a stable liquid thin film of a width similar or slightly lower than the droplet's width, $w \approx W$ (see Supporting Information, Movie S6). Since the PAPIDs used to form the regime map in Figure 2e have low viscosity (≈0.7 mPa s), we used gas shear-stress to achieve higher actuation velocities ($Ca > 2 \times 10^{-3}$), which are unattainable by surface inclination, required for the spreading droplet regime (Figure 2e, green cross symbols). The experimental transition velocity, taken as the minimal velocity that forms a stable spreading droplet film, was ≈80 mm s^{-1}.

2.3. Pattern Control

Looking at each flow regime separately, we analyzed the 3 applicative deposition patterns with respect to the influence of the main control parameters, such as actuation velocity and droplet volume, on related geometrical characteristics of the resultant patterns.

2.3.1. Dynamic Coffee-Ring Deposition Pattern

Similar to the well-known coffee stain theory, evaporative losses at the droplet-substrate contact line in the dynamic coffee-ring regime allow the free liquid surface to push the fluid to the perimeter of the droplet, causing the transport of solids to the contact line.[14] Nevertheless, since the droplet is in motion, only the 2 small segments of the contact line, parallel to the droplets velocity, U, are momentarily pinned to the surface, allowing sufficient time for solids to accumulate through evaporative deposition (**Figure 3**a). Consequently, 2 parallel line patterns are deposited tangentially to the 2 contact line segments. The 2 dynamic coffee-ring line patterns have characteristic ridge-shaped side profiles[23] (Figure 3b, top left and right), for which the width D_{DC} is on the order of single micrometers and peak height, h, on the order of nanometers, with h being proportional to D_{DC} (Figure 3b, bottom). Based on mass conservation and geometrical considerations, and by assuming triangular cross-section of the ridges (inset in Figure 3b, bottom), we predict that D_{DC} should scale with the droplet velocity, U, and trail width, W (proportional to the volume of the droplet) according to the Supporting Information, Section 4

$$D_{DC} \approx \left(\frac{WQ^2}{U^2}\right)^{1/3} \quad (2)$$

where Q (μm^2 s^{-1}) is the solids volumetric deposition rate per unit length of the contact-line, assumed to be constant. This scaling law is in a good agreement with our experiments with PAPIDs flowing down inclined surfaces. In fact, our experiments

show that the power law applies to all 3 flow regimes producing the dynamic coffee-ring double-ridge patterns, dynamic coffee-ring, μ-rivulet, and macro-rivulet regimes (Figure 3c).

2.3.2. μ-Rivulet Deposition Pattern

When a μ-rivulet is formed, the liquid emerging from the droplet's corner at the rear into the rivulet takes the form of two parallel contact lines. During evaporation, the distance between the contact lines slightly increases (see **Figure 4**a) probably as a result of a decrease in the surface tension and contact angle (see Supporting Information, Figure S1a) as the toluene/nonane ratio decreases. At these 2 contact lines deposition occurs until the liquid completely evaporates, leaving behind 2 parallel line patterns with a spacing of $w << W$ (Figure 4a). The 2 line patterns have characteristic ridge-shaped cross-sectional profiles (Figure 4b, top left and right), similar to the dynamic coffee-ring ridges, with a width, D_μ, and peak height, h_μ, of the order of micrometers and nanometers, respectively, and with h_μ being proportional to D_μ (Figure 4b, bottom part). The fast process (order of tens of milliseconds) of liquid deposition from the corner followed by complete evaporation takes the form of a stable rivulet with a receding evaporation front at the rear, maintaining a steady-state constant μ-rivulet length, L. Based on mass conservation and geometrical considerations, D_μ should scale with the droplet velocity, U, and the rivulet length, L, according to the Supporting Information, Section 5

$$D_\mu \approx \left(\frac{LJ}{U}\right)^{1/2} \tag{3}$$

where J (μm^2 s^{-1}) is the 2-dimensional evaporation flux assumed to be constant. Indeed, this relationship also agrees with our experiments of ink droplets flowing down inclined surfaces (Figure 4c, bottom x-axis). From similar considerations, and assuming that the height of the liquid left behind by the corner H_0 scales with w, we estimate that D_μ should also scale with w (see Supporting Information, Section 5)

$$D_\mu \approx w \tag{4}$$

This result is consistent with our experimental results (Figure 4c, top x-axis). Notably L and w are geometric characteristics of the μ-rivulet—both depending on U—and, probably also on ink properties, such as μ, γ, and droplet volume V. Interestingly, we can derive the following scaling between L, w, and the velocity U by combining (3) and (4)

$$J\frac{L}{w^2} \approx U \tag{5}$$

As supported by experiments (Supporting Information, Figure S7), this scaling shows that, as the velocity increases, the μ-rivulet becomes narrower and/or elongated. Although the details of the mechanism responsible for the formation of the μ-rivulet are without doubt complex and not yet understood, relationships (3), (4), and (5) offer a basic understanding of the relations between U, the main control parameter of the system, and the different geometric qualities of μ-rivulet deposition.

2.3.3. Spreading Droplet Deposition Pattern

When a spreading droplet thin film is formed, the liquid is pinned to the surface along 2 parallel contact lines. Deposition occurs at them until the liquid completely evaporates, leaving behind 2 parallel line patterns with a spacing of $w \approx W$ and a uniform thin-film deposit between the ridges (**Figure 5**a,b). The 2 line patterns have characteristic ridge shaped cross-sectional profiles (Figure 5c,d) with a width of the order of single micrometers and height of the order of tens of nanometers, while the thin-film deposit between them has a concave profile with a thickness of the order of single to tens of nanometers. Since the PAPID concentration changes during actuation, the pattern also has a unique lateral profile along the droplet actuation path in which both the thickness of the 2 ridges and the ridge spacing, w, increase in the direction of actuation (Figure 5e). Near the end of the pattern, the ridge height

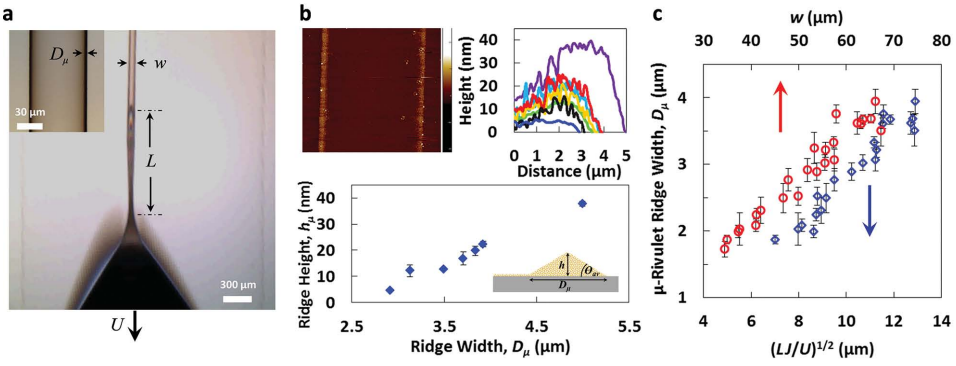

Figure 4. a) Optical micrograph of a PAPID flowing down an inclined Si wafer and leaving behind a μ-rivulet pattern of Au-NPs. μ-rivulet length (L), deposition pattern width (w), and droplet velocity (U) are depicted. The inset shows an enlargement of the μ-rivulet pattern with an indication of the ridge width (D_μ). b) AFM analysis of μ-rivulet deposition ridges showing (top left) a 60 × 60 μm scan of a characteristic NPs ridge (color scale ranging between 0–80 nm), (top right) height profiles of 7 representative ridges, and (bottom) maximum ridge height versus ridge width of the 7 ridges with the inset schematically illustrating a simplified triangular cross-section ridge profile. c) Plot showing D_μ versus $(L/U)^{1/2}J^{1/2}$ (bottom, x axis) and D_μ versus w (top, x axis) for ink droplets of different volumes ranges between 0.3–1.5 μL actuated at different surface inclinations between 18° and 45°.

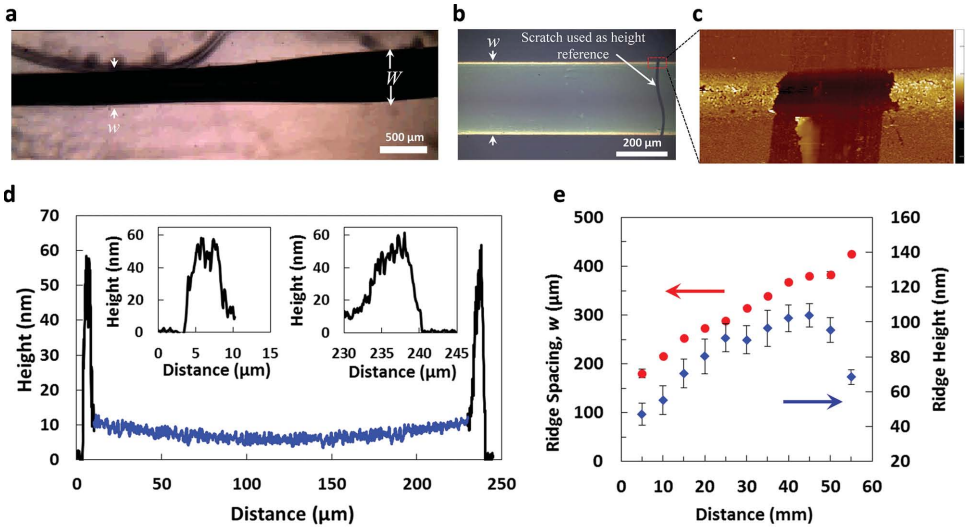

Figure 5. a) Optical micrograph of a 0.2 μL PAPID actuated from left to right over a glass slide by gas shear stress. b) Optical micrograph showing the resultant spreading droplet pattern after complete solvent evaporation, followed by a sintering process. c) A 40 × 20 μm AFM scan (color scale ranging between 0–200 nm) of the side ridge of the spreading droplet pattern. d) AFM cross-section thickness profile of a spreading droplet pattern, with the insets showing the 2 side ridges in scale and the blue line showing an assumed cross-section of the pattern's center (based on a second degree polynomial interpolation between the 2 ridge profiles and center thickness). e) Ridge height (red circles) and ridge spacing (blue diamonds) along the length of the pattern.

reaches a maximum and quickly decreases towards the center thickness. The thickness gradient and the overall length of the pattern depend on the volume of the droplet and the magnitude of the applied actuation force. These pattern characteristics can fabricate continuous line patterns with controlled thickness gradients that are important for devices based on functionally graded films.[24]

2.4. Effect of Surface Chemistry

Since the 3 applicative deposition mechanisms are evaporative deposition-related phenomena, we found that the hydrophobicity of the printed surface (Supporting Information, Figure S8a) that influences the contact angle with the PAPIDs affects the resultant patterns. PAPIDs form small contact angles (<14°) with hydrophilic to moderately hydrophobic surfaces, such as Si treated with UV and ozone, and Si covered with a self-assembled monolayer (SAM) of amine-terminated silanes, respectively (Supporting Information, Figure S8b). As a result, PAPIDs actuated over these surfaces form characteristic deposition patterns under the 3 applicative flow regimes: dynamic coffee-ring, μ-rivulet, and spreading droplet (Supporting Information, Figure S8c,d; Figure S8f,g; and Figure S8i,j, respectively). On the other hand, ink droplets form large contact angles (34°) with highly hydrophobic surfaces, such as Si covered with a SAM of alkane-backbone silanes (Supporting Information, Figure S8b). Thus, PAPIDs actuated over these surfaces do not undergo sufficient evaporative deposition, so no deposition pattern is formed under the dynamic coffee-ring regime (Supporting Information, Figure S8e). We also believe that due to an insufficient decrease in surface tension at the contact lines, pearling occurs under the μ-rivulet regime (Supporting Information, Figure S8h) and irregular line pattern are formed under the spreading droplet regime (Supporting Information, Figure S8k). Furthermore, the PAPIDs undergo coffee-ring pinning due to weaker Marangoni vortices, making much higher actuating forces necessary to initiate propulsion.

2.5. Applicability of Printing with PAPIDs

Control over the actuation velocity of PAPIDs makes it possible to print different functional line patterns through the 3 applicative deposition regimes over a variety of substrates. Since droplet bulk is in effect the ink reservoir, droplet volume limits the maximum pattern length (e.g., ≈8 cm for a 0.2 μL PAPID actuated using gas shear stress applied by a 5 L min^{-1} air flow). However, integration with robust and high resolution drop-on-demand dispensing systems[2] and accurate droplet actuation techniques[25] should resolve this constraint, increase printing resolution and enable fabrication of array patterns. We used surface inclination to actuate Au NPs-based PAPIDs to obtain conducting patterns that can be used as printed circuit lines. For example, two semitransparent, μ-rivulet patterns were printed on the inside surface of a glass vial using two PAPIDs actuated by surface inclination (**Figure 6**a–c). After sintering, the resultant gold lines were used to power a commercial red LED positioned at the bottom of the vial (Supporting Information, Movie S7). The sintering process (Supporting Information, Figure S9) enhanced conductivity[1] (Figure 6d), achieving a resistivity of 0.13 μΩm, i.e., ≈5 times the resistivity of bulk gold. This example illustrates the unique capability of PAPID to print functional patterns on curved surfaces with restricted spatial access. Under similar conditions, but at a lower surface inclination (≈15°), dynamic coffee-ring patterns of gold were printed over a Si wafer (Supporting Information, Figure S10a–c) and a flexible polyethylene foil (Supporting

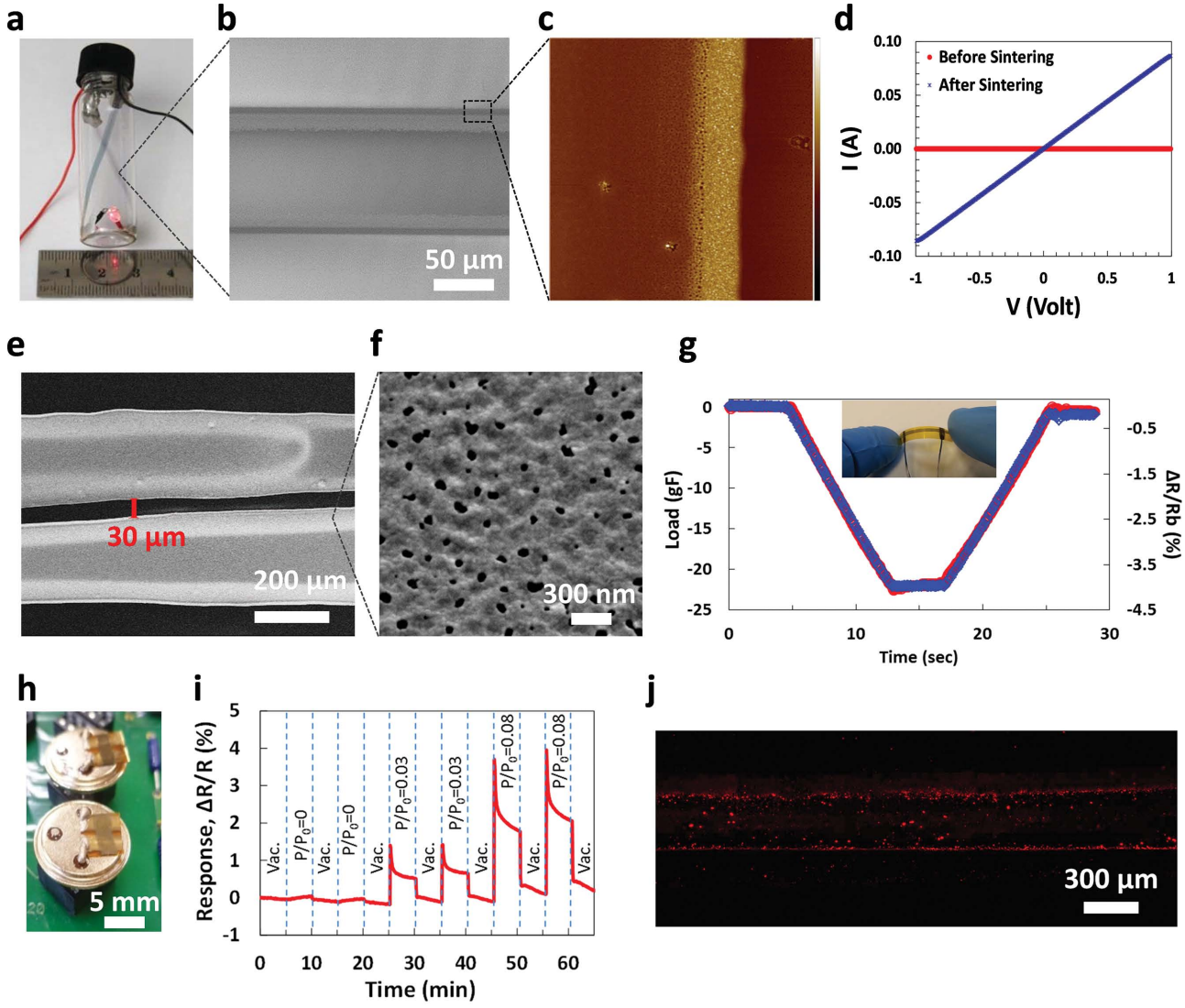

Figure 6. a) Optical micrograph of 2 semitransparent sintered gold µ-rivulet patterns printed on the inside surface of a 5 mL glass vial using 2 0.4 µL PAPIDs of 10 wt% decanethiol capped Au-NPs ink actuated by surface inclination (≈35°) and used to supply power (4.5 V) to a commercial red LED positioned at the bottom of the vial. b) HR-SEM image of one of the µ-rivulet patterns powering the LED. c) A 20 × 20 µm AFM scan of a ridge segment of the µ-rivulet pattern (color scale range from 0–80 nm) having a roughness of ≈5 nm. d) An *I*/*V* scan before (red) and after (blue) sintering of the 2 µ-rivulet patterns. e) HR-SEM image of 2 parallel micro-electrodes with ≈30 µm spacing printed over a glass slide by gas shear stress actuation of two ≈0.2 mL PAPIDs. f) HR-SEM image showing the continuous morphology of the microelectrodes after sintering. g) Plot showing the overlap between the load versus time curve (blue) and the resistance response versus time curve (red) of a 1 cm long strain sensor fabricated over a polyimide (Kapton) foil through the 4-step fabrication process (Supporting Information, Section 8). Inset shows an optical micrograph of the strain sensor. h) Optical micrograph showing 2 chemiresistors fabricated over a polyimide (Kapton) foil through the 4-step process. i) Plot showing the resistance response of a chemiresistor to duplicate 5 min exposure cycles to increasing concentrations of 2-ethylhexanol. j) Confocal microscope image of a spreading droplet pattern of CdTe quantum dots printed over a glass slide through gas shear stress actuation of a 0.2 µL PAPID.

Information, Figure S11a). Since polyethylene foils undergo substantial thermal deformation at high temperatures, an ink of dodecylamine capped Au NPs was used to allow low temperature sintering at only 80 °C (Supporting Information, Figure S11b–d).

We could also produce parallel spreading droplet patterns with a width of ≈200 µm and spacing down to 30 µm (Figure 6e) by actuating PAPIDs using gas shear stress actuation over different types of substrates. After sintering, these patterns became continuous Au films (Figure 6f) with a sheet resistance of ≈5 Ω sq^{-1}, and were used as printed microelectrodes. The sintering process also enabled connecting or overlapping between printed patterns that would otherwise dissolve one another in the overlapping regions. Harnessing these concepts, a simple four-step process was used to fabricate sensor devices (Supporting Information, Figure S12). Using this process, highly sensitive strain sensors for the detection of load[26] and chemiresistors for the detection of volatile organic compounds[27] were successfully made over a polyimide (Kapton) foil (Figure 6g and Figure 6h,i, respectively). Finally, a photonic

ink based on CdTe quantum dots (see Experimental Section) was used to form fluorescent spreading droplet line patterns over glass slides through gas shear stress actuation (Figure 6j). These examples demonstrate the potential of printing with PAPIDs as a useful tool for printed electronics, sensors, and photonic devices.

3. Summary and Conclusions

The ability to print nanomaterials over planar or curved surfaces with limited spatial access, and the flexibility to choose between and control 2 distinct, truly continuous line patterns simply by adjusting droplet size and actuation velocity, creates design options unattainable with conventional techniques. Creating controlled thickness gradient along the length of printed line patterns should be attractive for producing functionally graded devices.[24] Using simple bench-top droplet actuation techniques, such as gas shear stress, PAPIDs enable device fabrication at ambient conditions with pattern resolutions down to tens of micrometers. Due to the dynamic nature of this patterning approach, future research into the dynamics inside the PAPID should be interesting regarding directional self-rearranging of the nanomaterials, especially 2D nanomaterials.[28,29] The compatibility of the approach with thin flexible substrates alongside resolution enhancement through integration with high resolution dispensing systems and accurate droplet actuation techniques should create new fabrication opportunities for flexible electronic applications.

4. Experimental Section

Materials: Au-NPs capped with a monolayer of decanethiol, hexanethiol, or dodecylamine ligands were synthesized through the Brust method,[30] achieving colloidal toluene solutions. These solutions were purified through precipitation in ethanol followed by centrifugation at 4000 rpm for 10 min, before being dissolved back by toluene, achieving concentrated Au-NPs toluene solutions. Functional inks were produced by diluting the concentrated Au-NPs toluene solutions with toluene and an additional solvent (e.g., nonane or octane) to achieve the desired Au-NPs concentration and binary composition. Unless otherwise indicated in the text, PAPIDs were Au-NP-based ink with a composition of 5 wt% of decanethiol capped Au-NPs and a 4:1 toluene/nonane volume ration. CdTe quantum dots (QDs) were synthesized following the procedure of Kloper et al.[31] achieving red fluorescent CdTe-QDs with a characteristic absorption peak at 612 nm (Supporting Information, Figure S13).[31] A functional CdTe-QDs based ink was produced by diluting the concentrated CdTe-QDs toluene solution with toluene and nonane to achieve 2 wt% of CdTe-QDs and a 7:3 toluene/nonane volume ratio. All organic reagents and chemicals employed for synthesis, ink preparation, or volatile organic compound (VOC) generation were analytical grade materials obtained from Sigma-Aldrich, Israel. Kapton-HN (50 μm thick) and polyethylene (100 μm thick) substrates were obtained from DuPont (through GADOT).

Procedures: Prior to use, all substrates were cleaned by rinsing in acetone, methanol, and 2-propanol, followed by drying in a stream of nitrogen, rinsing in double-distilled water and finally drying in another stream of nitrogen. Treatment with high intensity UV light and ozone was done with a Novascan PSD Pro UV Ozone system. To functionalize Si substrate surfaces with SAMs of either amine-terminated silanes or alkane-backbone silanes, the Si substrates were first etched using oxygen plasma (50 w) for 5 min before reaction with a $\approx 5 \times 10^{-3}$ M chloroform-based solution of 3-aminopropyltrimethoxysilane or trichlorooctadecylsilane, respectively.[29]

Gas Shear Stress Actuation: Actuation of PAPIDs using gas shear stress was achieved by directing an air-flow through a milli-channel over the droplets, using a vacuum pump with a flow controller (Supporting Information, Figure S14a,b). Unless otherwise stated in the main text, gas shear stress actuation was done with an airflow of 5 L min^{-1}, which induces an overhead airflow with a velocity of ≈5.5 m s^{-1}. In order to enable gas shear stress actuation of a large number of ink droplets with a wide size distribution, we used a custom built electrospraying apparatus operated at room temperature with a voltage of 2.5 kV between a syringe needle (0.5 mm in diameter) and a grounded collector plate placed 25 mm under the needle tip.[32]

Characterization: Small-scale distance measurements of the different pattern features (e.g., μ-rivulet ridge widths, w) were measured using a Nikon Eclipse LV150N optical microscope (with 150× bright field objective). Top view movies of flowing droplets and large-scale distance measurements (e.g., dynamic coffee-ring pattern width, W) were taken using an Optika B-350 optical microscope (with ×4 bright field objective). Resistance response of resistive sensors (strain sensors and chemiresistors) was calculated as the percent change in resistance with respect to the baseline resistance of the sensor. The Au-NP-based chemiresistors were characterized by monitoring their resistance response to duplicate 5 min exposure cycles to mixtures of nitrogen with increasing concentrations of 2-ethylhexanol, as a representative volatile organic compound (VOC). A typical exposure cycle, carried out inside a 330 cm^3 stainless-steel chamber, involved a 5 min vacuum (<50 mTorr) baseline step, followed by 5 min exposure to the test mixture under stagnant conditions, and ended with another 5 min vacuum step, while each successive acquisition cycle of all the tested sensors was completed in <5 s. The concentrations of the exposure cycles were calculated in terms of the VOC's vapor pressure (P) relative to its saturation vapor pressure (P_0). The gaseous mixtures were produced using a commercial permeation/diffusion tube dilution (PDTD) system (Umwelttechnik MCZ, Germany). Purified dry nitrogen (>99.99%) from a commercial nitrogen generator (N-30, On Site Gas Systems, USA) equipped with a nitrogen purifier was used as a carrier gas. The PDTD system used a temperature controlled oven to mix a constant flow (200 ± 1 cm^3 min^{-1}) of purified nitrogen with a constant mass flow of a vaporized VOC exiting a diffusion tube (Dynacal, VICI Metronics). The nitrogen/VOC mixture exiting the PDTD system was diluted again with nitrogen to achieve the desired concentrations. The VOC concentration was determined by controlling the mass flow-rate of the vaporized VOC (by the temperature of the diffusion tubes) and the total volumetric nitrogen flow rate. The concentrations were verified using a commercial portable photo ionization detector (VOC-TRAQ, Bronze piD-TECH plus, Baseline-Mocon Inc., USA). A Keithley data logger device (model 2701 DMM) controlled by a custom Labview program was used to sequentially acquire resistance readings from the chemiresistors. Constant currents in the range of 0.7–1 × 10^4 μA were used for resistance measurements. Strain sensors were characterized by measuring their resistance response to load. A Mark-10 ESM301 motorized test-stand was used to apply strain in a constant speed of 1.5 mm s^{-1}. The strain was applied to the strain sensor by an upper beam, while the sensor is supported by 2 parallel bottom beams (downward arrow and bottom gray beams in Supporting Information, Figure S15, respectively). Under an applied stress, the sensor's substrate is bent. The outer (upper) surface is then subjected to compression, while the inner (lower) surface is under dilatation. The forces were measured by an Advanced Digital Force Gauge (Mark-10 USA). The electrical resistance of the sensing layer (gray layer in Supporting Information, Figure S15) was measured through to electrical wires (red and black lines in Supporting Information, Figure S15) by a Keithley data-logger device (model 2701DMM) controlled by a custom Labview program. High resolution scanning electron microscope (HR-SEM) images were acquired using a Zeiss Ultra-Plus FEG-SEM with an in-lens secondary electron detector and acceleration energies ranging between 1 and 4 keV. Atomic force microscope (AFM) analysis used a NanoWizard

3 NanoScience AFM with TopViewOptics (JPK Instruments AG, Germany) in tapping mode. Contact angle and surface tension measurements were carried out with an Attension-Theta device (by Biolin Scientific). QDs patterns were visualized with a confocal microscope LSM510 at 488 nm excitation and fluorescence detection at >575 nm.

Supporting Information

Supporting Information is available from the Wiley Online Library or from the author.

Acknowledgements

The research received funding from Phase-I (Grant ID: OPP1058560) and Phase-II (Grant ID: OPP1109493) Grand Challenges Explorations award of the Bill & Melinda Gates Foundation. The authors acknowledge and thank R. Edrie and E. Kessleman for help with AFM analysis; B. Pokroy and B. Haimov for help with contact angle measurements; Y. Paz and N. S. Waldman for help with electrospray deposition; E. Lifshitz and D. Yanover for help with obtaining QDs; V. Kloper for NPs synthesis; M. Kalina and A. Brenner for help with HR-HR-SEM imaging; M. Segev-Bar for help with strain sensor fabrication; E. Homede and M. Abo-Jabal for help with surface modifications.

Received: January 19, 2015
Revised: February 19, 2015
Published online: March 16, 2015

[1] H. H. Lee, K. S. Chou, K. C. Huang, *Nanotechnology* **2005**, *16*, 2436.
[2] J.-U. Park, M. Hardy, S. J. Kang, K. Barton, K. Adair, D. K. Mukhopadhyay, C. Y. Lee, M. S. Strano, A. G. Alleyne, J. G. Georgiadis, P. M. Ferreira, J. A. Rogers, *Nature Mater.* **2007**, *6*, 782.
[3] D. A. Pardo, G. E. Jabbour, N. Peyghambarian, *Adv. Mater.* **2000**, *12*, 1249.
[4] R. Parashkov, E. Becker, T. Riedl, H.-H. Johannes, K. Wolfgang, *Proce. IEEE* **2006**, *93*, 1321.
[5] S. R. Forrest, *Nature* **2004**, *428*, 911.
[6] S. H. Ko, H. Pan, C. P. Grigoropoulos, C. K. Luscombe, J. M. J. Frechet, D. Poulikakos, *Nanotechnology* **2007**, *18*, 345202.
[7] F. Torrisi, T. Hasan, W. Wu, Z. Sun, A. Lombardo, T. S. Kulmala, G.-W. Hsieh, S. Jung, F. Bonaccorso, P. J. Paul, D. Chu, A. C. Ferrari, *ACS Nano* **2012**, *6*, 2992.
[8] E. Chow, J. Herrmann, C. S. Barton, B. Raguse, L. Wieczorek, *Anal. Chim. Acta* **2009**, *632*, 135.
[9] F. C. Krebs, M. Jorgensen, K. Norrman, O. Hagemann, J. Alstrup, T. D. Nielsen, J. Fyenbo, K. Larsen, J. Kristensen, *Solar Energy Mater. Solar Cells* **2009**, *93*, 422.
[10] S. B. Fuller, E. J. Wilhelm, J. M. Jacobson, *J. Microelectromech. Sys.* **2002**, *11*, 54.
[11] S.-I. Park, Y. Xiong, R.-H. Kim, P. Elvikis, M. Meitl, D.-H. Kim, J. Wu, J. Yoon, C.-J. Yu, Z. Liu, Y. Huang, K.-c. Hwang, P. Ferreira, X. Li, K. Choquette, J. A. Rogers, *Science* **2009**, *325*, 977.
[12] C. Kim, M. Nogi, K. Suganuma, Y. Yamato, *ACS Appl. Mater. Interfaces* **2012**, *4*, 2168.
[13] B. Y. Ahn, E. B. Duoss, M. J. Motala, X. Guo, S.-I. Park, Y. Xiong, J. Yoon, R. G. Nuzzo, J. A. Rogers, J. A. Lewis, *Science* **2009**, *323*, 1590.
[14] R. D. Deegan, O. Bakajin, T. F. Dupont, G. Huber, S. R. Nagel, T. A. Witten, *Phys. Rev. E* **2000**, *62*, 756.
[15] H.-Y. Kim, H. J. Lee, B. H. Kang, *J. Col. Interface Sci.* **2002**, *247*, 372.
[16] A. Oron, S. H. Davis, S. G. Bankoff, *Rev. Mod. Phys.* **1997**, *69*, 931.
[17] S. Bekki, M. Vignes-Adler, E. Nakache, P. M. Adler, *J. Col. Interface Sci.* **1990**, *140*, 492.
[18] D. Pesach, A. Marmur, *Langmuir* **1987**, *3*, 519.
[19] H. Hu, R. G. Larson, *J. Phys. Chem. B* **2006**, *110*, 7090.
[20] J. Park, J. Moon, *Langmuir* **2006**, *22*, 3506.
[21] J. H. Snoeijer, N. Le Grand-Piteira, L. Limat, H. A. Stone, J. Eggers, *Phys. Fluids* **2007**, *19*, 042104.
[22] L. M. Hocking, *J. Fluid Mech.* **1990**, *211*, 373.
[23] R. Bhardwaj, X. Fang, D. Attinger, *New J. Phys.* **2009**, *11*, 075020.
[24] M. Segev-Bar, G. Konvalina, H. Haick, *Adv. Mater.* **2015**, DOI: 10.1002/adma.201405224.
[25] A. A. Darhuber, S. M. Troian, *Annu. Rev. Fluid Mech.* **2005**, *37*, 425.
[26] M. Segev-Bar, H. Haick, *ACS Nano* **2013**, *7*, 8366.
[27] G. Konvalina, H. Haick, *ACS Appl. Mater. Interface* **2011**, *4*, 317.
[28] M. Bashouti, W. Salalha, M. Brumer, E. Zussman, E. Lifshitz, *ChemPhysChem* **2006**, *7*, 102.
[29] O. Assad, A. M. Leshansky, B. Wang, T. Stelzner, S. Christiansen, H. Haick, *ACS Nano* **2012**, *6*, 4702.
[30] M. Brust, M. Walker, D. Bethell, D. J. Schiffrin, R. Whyman, *J. Chem. Soc. Chem. Commun.* **1994**, *7*, 801.
[31] V. Kloper, R. Osovsky, J. Kolny-Olesiak, A. Sashchiuk, E. Lifshitz, *J. Phys. Chem. C* **2007**, *111*, 10336.
[32] M. Cloupeau, B. Prunet-Foch, *J. Aerosol Sci.* **1994**, *25*, 1021.